



Molecularly imprinted sol-gel/Au@Ag core-shell nano-urchin localized surface plasmon resonance sensor designed in reflection mode for detection of organic acid vapors

Bin Chen^{a,*}, Hao Guo^b, Chuanjun Liu^b, Liang Shang^b, Xiao Ye^b, Lin Chen^b, Changhao Feng^a, Kenshi Hayashi^{b,**}

^a Chongqing Key Laboratory of Non-linear Circuit and Intelligent Information Processing, College of Electronic and Information Engineering, Southwest University, Chongqing, 400715, PR China

^b Department of Electronics, Graduate School of Information Science and Electrical Engineering, Kyushu University, Fukuoka, 819-0395, Japan



ARTICLE INFO

Keywords:

Localized surface plasmon resonance
Molecularly imprinted sol-gel
Biogenetic volatile organic compound
Vapor clustering

ABSTRACT

A molecularly imprinted sol-gel (MISG)/Au@Ag core-shell NU sensor is proposed for organic vapor detection in an optical fiber-based reflection mode. The compact structure design of the system in the reflection model is promising for practical use as a portable and rapid responsivity sensing probe. Volatile organic acids (OAs) are analogs to biogenetic volatile organic vapors related to specific human diseases. Here, Au@Ag core-shell nano-urchins exhibiting branched tips were synthesized and deposited on indium tin oxide (ITO) glass in small dimer and trimmer clusters to generate an enhanced electric field. A MISG solution was then spin-coated on the substrate to fabricate MISG-LSPR sensors, and three types of MISGs were developed for the detection of hexanoic acid, heptanoic acid and octanoic acid. The normalized spectral response indicated selectivity of the MISG-LSPR sensors for the corresponding template OAs. With Native Bayes and linear discriminant analysis of the sensor responses, where the latter were detected by the proposed system, single- and mixed-OA vapors could be classified into separate clusters. This signified that the proposed MISG-LSPR sensor can be applied toward pattern recognition of single vapors or multiple vapor mixtures.

1. Introduction

Localized surface plasmon resonance (LSPR) results from the plasmonic resonance of noble metallic nanoparticles (NPs), and is sensitive to changes in the surrounding refractive index (RI) (Willets and Duyne, 2007; Shen et al., 2013). The advantages of LSPR sensors are their high sensitivity, rapid response, and high stability (Mayer; Hafner, 2011; Pai et al., 2017). However, bare NPs lack the capacity for specific selectivity. Molecularly imprinted polymer (MIP) is an effective method for the production of polymeric artificial receptors for specific molecular recognition (Uzun and Turner, 2016; Wackerlig and Schirhagl, 2016; Tiwari and Prasad, 2015; Kong et al., 2017). By adding template molecules in the synthesis process, nanoscale cavities similar to the template molecules are generated (Zhang et al., 2017; Wackerlig and Schirhagl, 2016; Tiwari and Prasad, 2015). In our previous work, MIP of terpenes were spin-coated on AuNPs on quartz glass as the MIP/AuNPs sensor (

Chen et al., 2016, 2020bib_Chen_et_al_2016abib_Chen_et_al_2020). Tuning the polymer thickness and the shape of AuNPs achieved a balanced performance of sensitivity and selectivity. The sensing performance of these sensors was measured in a transmission mode (Scheme 1(a)), wherein the light source and the detection unit are located at the two ends of the sensing cell. Therefore, to decrease the optical signal loss and maintain sensing reproducibility, a fixing frame is necessary to connect the light source and detection unit and fix their relative position. Typically, the fixing frame is used as the sensing cell where a certain volatile organic compound (VOC) concentration occurs. However, this type of design limits the practical application of the sensor as a portable sensing probe.

Optical sensing systems can be analyzed with respect to reflection, transmission, scattering, and absorption modes (Yan et al., 2018). For example, the absorption spectrometer is designed to operate in a transmission mode, where light passing through the sensing cell is

* Corresponding author.

** Corresponding author.

E-mail addresses: chenbin121@swu.edu.cn (B. Chen), hayashi@ed.kyushu-u.ac.jp (K. Hayashi).

received by the detector. Hence, the sensing film should be transparent or semi-transparent. In reflection mode, a particularly common sensing modality uses a thin metallic film deposited on the surface of a prism. Thus, light striking the film surface from the prism side at an incident angle greater than the critical angle undergoes total internal reflection (TIR) and can excite film surface plasmons via coupling to the evanescent fields associate with the TIR light (Mock et al., 2012; Ciraci et al., 2012). In this way, small changes to the RI over the entire measured surface of the metal film are measurable. However, application of this design is limited to laboratory use and is expensive. In recent years, optical fibers have been selected to establish the sensing system because of the advantages of fiber optic-based LSPR sensors such as portability, low cost, small size, and simple optical set-up (Kim et al., 2019; Lee et al., 2018). As shown in Scheme 1 (a), for real-field VOC detection, a device designed in the reflection mode is very portable with an easy-to-move sensing probe.

In the present work, an optical fiber-based reflection mode sensing system is proposed for organic acid (OA) vapor detection. The OAs are naturally produced during the metabolic process of different organisms (Tsoukalas et al., 2017; Liu et al., 2018). OAs are intermediate metabolites of critical metabolic pathways, such as the Krebs cycle, carbohydrate metabolism, and ketone body metabolism (Usami et al., 2011; Lederer et al., 2017). For example, a preoperative fecal OA profile has been approved as having a clinically important impact on the incidence of postoperative infectious complications in patients undergoing major hepatectomy with extrahepatic bile duct resection (Yokoyama et al., 2017; Miekisch et al., 2004; Kolk et al., 2012). As the main byproducts of metabolic processes of certain bacteria, volatile OAs can be considered as biogenetic VOCs related to specific diseases. Here, Ag@Au core-shell NUs were synthesized for detection of VOC-induced RI change. By controlling the amount of AgNO₃, we obtained Au@Ag core-shell NUs that maintained sharp tips and deposited on ITO glass slides. The spectral peak shifts ($\Delta\lambda$) in various environmental permittivity values were compared to identify the optimal refractive index sensitivity (RIS, $\Delta\lambda$), and sensing films with this optimized RIS was selected. Three types of molecularly imprinted sol-gel (MISGs), including hexanoic acid (hex), heptanoic acid (hep) and octanoic acid (oct), were spin-coated on the optimized substrate and were applied as MISG-LSPR sensors. The experimental results showed that the response of these MISG-LSPR sensors to the corresponding OA vapor was selective. The response of MISG-LSPR sensors to a mixture of OA vapors was analyzed by principal component analysis (PCA), linear discriminant analysis (LDA), K-nearest neighbors (KNN) and Native Bayes (NB) method for odor recognition and classification. The feasibility of the proposed MISG-LSPR sensors combined with LDA and NB methods was effective for OA vapors classification. The objective of this study is to develop a new sensing strategy for VOC detection in medical diagnosis.

2. Experimental

2.1. Materials

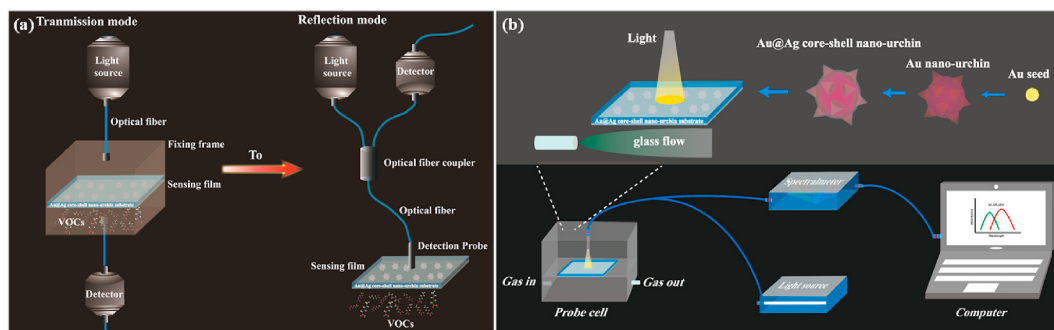
Hex, hep, oct, 1,5-pentanediol, titanium tetrabutoxide (TBOT), isopropanol, titanium tetrachloride (TiCl₄), acetone, trisodium citrate, hydroquinone, silver nitrate (AgNO₃), polyvinylpyrrolidone (PVP-K30), and ethanol were purchased from Wako Pure Chemical Industries Co., Ltd. (Osaka, Japan). (3-mercaptopropyl) trimethoxysilane (APTES) was purchased from Shin-Etsu Chemical Co., Ltd (Tokyo, Japan). HAuCl₄·3H₂O was purchased from Sigma-Aldrich (St. Louis, MO, USA). All reagents were used as received.

2.2. Instrumentation

Scanning electron microscopy (SEM, SU8000, Hitachi, Japan) and transmission electron microscopy and EDX (TEM, H-7650, Hitachi) were used to image sensor morphologies. Absorbance spectra were recorded with an ultraviolet-visible (UV-vis) spectrophotometer (UV1800, Shimadzu, Japan) for spectral calibration. The reflection mode optical system included a tungsten-halogen light source (HL-2000, Ocean Optics, USA), a sensing cell, and an UV-vis spectrometer (Flame-S, Ocean Optics, USA), with OPwave + software (Ocean Optics, USA). The sensing cell was produced by 3D printer (UltimakerS5, Japan). A spin-coater (MS-B100, Opticoat, Japan) was utilized to fabricate MISG films. PCA, LDA, NB, and KNN analysis were performed with R (version 3.4.3), and the finite-difference time-domain (FDTD) simulations were performed using a commercial simulation program (FDTD solutions 8.11.422 by Lumerical Solutions). In the simulation, a total-field scattered-field light source with a wavelength of 400–1000 nm was propagated along the z-axis and perpendicular to the x-y plane of the Au@Ag core-shell NUs and a perfectly matched layer was involved in all boundary conditions. The override mesh cell size used was 1 × 1 × 1 nm³.

2.3. Synthesis of Au@Ag core-shell NUS

First, Au NUs were synthesized as the templates for Ag shell growth according to the previously reported method (Chen et al., 2017). Typically, the Au NUs were grown by sequentially adding 25 µL of 100 mM aqueous HAuCl₄, the prepared gold seed solution (50 µL), 22 µL of 1 w/v % trisodium citrate aqueous solution, and 1000 µL of 30 mM hydroquinone into 9.6 mL of deionized water with vigorous stirring for 30 min. The Ag shell was deposited in situ on the prepared Au NU templates through a polyol process. A pentanediol solution of PVP-K30 (20 mg/mL) and AgNO₃ (10 mg/mL) were prepared, and the as-prepared Au NUs were re-dispersed in the pentanediol (6 mL), ultrasonicated, and agitated by a vortex (absorbance value 3.3). Subsequently, the PVP solution (2 mL) and AgNO₃ (0.3–0.9 mL) were injected and stirred thoroughly. Finally, the mixture was transferred to a Teflon-lined stainless-steel autoclave and heated to 150 °C for 30 min. The obtained



Scheme 1. (a) Schematics of the transmission (left) and reflection (right) modes. (b) Schematics of the proposed reflection mode vapor-sensing system.

mixture containing Au@Ag core-shell NUs was naturally cooled, separated by centrifugation, and re-dispersed first in ethanol and then deionized water.

2.4. Preparation of MISG solutions

The MISG solutions were prepared as previously reported (Chen et al., 2020; Shang et al., 2018a,b). Here, TBOT (135 μL) was dissolved in 2 mL of isopropanol, whereupon hex, hep, or oct (50 μL) as a template material and 50 μL of APTES were sequentially added with stirring. Then, 25 μL of TiCl₄ was added to initiate the MISG solution, after which the MISG solution was pre-hydrolyzed in a water bath at 60 °C for 1 h with stirring. The mixture was then vigorously stirred for 8 h at room temperature before spin coating.

2.5. Fabrication of MISG-coated Au@Ag core-shell NUs sensors

Pre-cleaned ITO glass substrates were immersed in a 1: 20 vol ratio of an APTES/ethanol solution for 2 h, ultrasonically washed with ethanol three times, and then dried in a nitrogen stream. The surface-modified substrates were tiled at the bottom of a glass dish. By controlling the deposition time of the prepared Au@Ag core-shell NUs solutions, slides with well-defined NU densities of were prepared. The amine (-NH₂) groups of APTES help to capture Au@Ag core-shell NUs via Au-N bonds. The MISG and NISG mixture was then spin-coated onto the slide and heated at 60 °C for 8 h to complete MISG fabrication and OA template vapor evaporation. The samples were stored in vacuum prior to spectral analysis.

2.6. Vapor generation and detection platform

The reflection mode sensing system proposed in this study is as shown in Scheme 1 and Fig. S1. The absorption spectra of the MISG-LSPR sensor in air and in OA vapor were recorded. Light was irradiated from the opposite side of the ITO substrate to guarantee that the front side of ITO substrate could maintain sufficient contact with the OA vapor flow. The OAs and their mixture were generated in the home-made vapor-sensing cell, where the OA vapor was generated from a glass bottle with odorants (2 mL) via the headspace method. The vapor concentrations were calculated by

$$C = \frac{k \times D_r \times 10^3}{F} \quad (1)$$

where D_r is the diffusion rate (μg/min), F is the flow rate of the dilute air (L/min), and k is the factor used to convert vapor weight to volume, calculated by

$$k = \frac{22.4 \times (273 + t) \times 760}{M \times 273 \times P} \quad (2)$$

where M is the molecular weight, t is the temperature in the gas chamber (°C), and P is the gas pressure (760 mmHg). Vapor responses were recorded for a 600 s vapor flow. The concentrations of the target OA vapors of hex, hep, and oct were calculated to be 40.93, 21.05, and 11.23 ppm, respectively, under an air flow of 0.5 L min/L.

3. Results and discussion

3.1. Synthesized Au@Ag core-shell NUs

The synthesis strategy for Au@Ag core-shell NUs was based on the gradual reduction of Ag⁺ ions via addition of AgNO₃ to a solution containing preformed citrate-stabilized Au NPs and a reducing agent PVP. The normalized absorbance spectra of the Au@Ag core-shell NUs are shown in Fig. S2. Compared with the template NUs, the LSPR band of the Au@Ag core-shell NUs was blue-shifted and the spectral bandwidth was

widened. Both of these phenomena could be explained by increased particle volume and the dielectric properties of silver. However, with further increase of the amount of AgNO₃, the spectral bandwidth became narrowed again, which may be ascribed to the generation of small-sized Ag NPs as a by-product (Fig. S3 (d)).

The morphologies of the prepared Au@Ag core-shell NUs are illustrated in Fig. S4. As shown in Fig. S4 (a), the average Au NU size is approximately 140 nm. With an increasing amount of AgNO₃, the center part of the NUs became larger and the tips of the NUs were somewhat blunt. Higher-resolution TEM images of the spiky Au@Ag core-shell NUs (Fig. S3) further confirmed that the tips of the core-shell structure were still sharp with increased addition of AgNO₃, while small Ag NPs were observed as a by-product with excessive AgNO₃. Chemical analyses via energy-dispersive X-ray spectroscopy (EDX) on elemental Au and Ag elements (Fig. 1) indicated that a monodispersed alloy was formed. Additionally, a preferential Ag deposition on the central part of the Au NUs was observed. Furthermore, the EDX spectra in Fig. 1(e) and (j) and 1(o) showed that the Ag shell thickness increased with increasing Ag content ratio.

The electric field distribution around Au@Ag core-shell NUs vs Ag shell thickness was simulated using FDTD (Fig. S5). The results indicated that a similar electric field enhancement was found for the spiky Au@Ag core-shell NUs as the Ag shell increased to 10 nm (Fig. S5 (a-e)). Conversely, when the Ag tips become wide (i.e., blunt), electric field enhancement noticeably decreased (Fig. S5 (f-h)).

3.2. Optical characteristics of Au@Ag core-shell NUs on ITO glass

The Au@Ag core-shell NUs were deposited on ITO glass and the absorption spectra were recorded, as shown in Fig. S6(a). Three spectral peaks were present, where the first spectral peak located at ~340 nm was attributed to the thin Ag shell, the second spectral peak at ~575 nm was attributed to the LSPR dipole polarization from the Au@Ag core-shell NUs, and the third peak at ~863 nm was attributed mainly to the coupling effects among the NUs. Herein, the deposition density of the Au@Ag core-shell NUs on ITO glass slides was controlled by changing the deposition time in the NUs solution. As illustrated Fig. S6 (a), when deposition time increased, absorbance of all three peaks increased. Compared with our previous work (Chen et al., 2020), the spectral peaks were red-shifted. There are two main reasons to explain this phenomenon: First, the Au@Ag core-shell NUs were bigger than the Au NUs (Fig. 1). The second reason is ascribed to an effect from the ITO substrate.

The RIS of the substrate with varying deposition time was investigated (Fig. S6 (b)), and the differences between substrate spectral peaks in air and water were compared and used to evaluate the RI sensing ability. Typical spectra of Au@Ag core-shell NUs deposited on ITO glass in air and water are shown in Fig. S7. The results showed that all three peaks were sensitive to the RI change, though the second and third peaks were very sensitive and were stable to the RI change (from air to water). The first spectral peak was unstable, which may be because the position of the first peak is much closer to the ultraviolet band than the other two peaks. The SEM images of Au@Ag core-shell NUs deposited on ITO glass were investigated (Fig. 2). The NU density increased with increasing deposition time. In Fig. 2 (a) and 2(b), the NUs were distributed as small-sized clusters such as dimers, trimers or tetramers, where the NU cluster size increased with increasing deposition time. The RIS (and especially the Δλ₃ red-shift) decreased when the NU clusters increased in size, which may be explained by the electric field coupling effect among Au NPs (Halas et al., 2011; Wustholz et al., 2010). Here, we suggest that the small-sized NU clusters contributed to a larger spectral red-shift (Δλ₃), while the large-sized NU clusters induced the opposite effect. Hence, 5 h was chosen as the optimal deposition time for the following experiments.

The electric field distribution around the Au@Ag core-shell NUs was simulated using FDTD, as shown in Fig. 3. When the inter-NU distance of

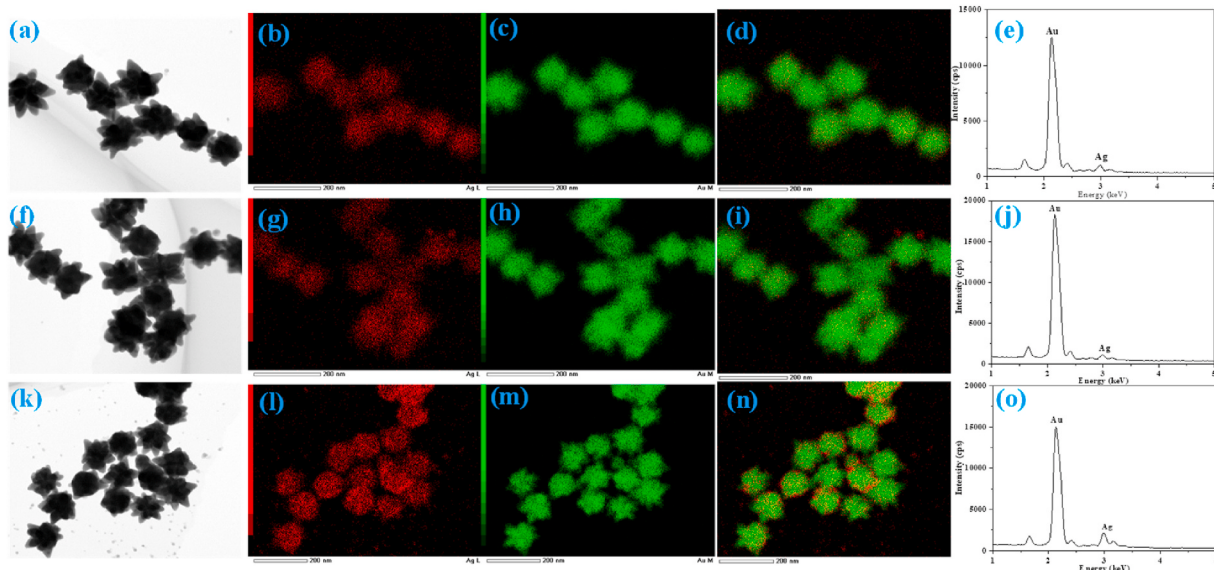


Fig. 1. (a, f, k) TEM images and corresponding elemental mapping of (b, g, l) Ag, (c, h, m) Au and (d, i, n) combined Au/Ag mapping. (e, j, o) EDX spectra of spiky Au@Ag core-shell NUs versus content ratio of AgNO_3 .

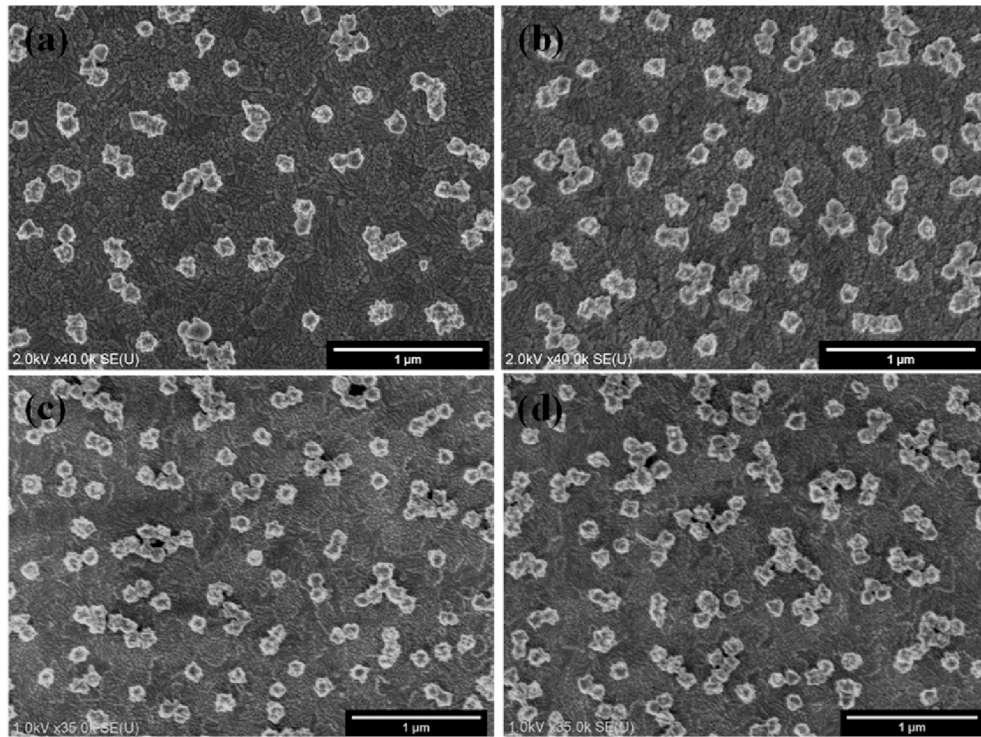


Fig. 2. SEM images of Au@Ag core-shell NUs on ITO glass with a deposition time of (a) 4 h, (b) 6 h, (c) 8 h, (d) 10 h.

an NU dimer was as small as 5 nm, an enhanced electric field was clearly generated among the NUs. Moreover, the electric field hot spot was extremely enhanced when the NU dimer was deposited on ITO glass (Fig. 3(d)), which is consistent with our experimental results.

3.3. Gas sensing characteristics of MISG-LSPR sensor

The absorption spectra of the system comprising an MISG layer spin-coated on a Au@Ag core-shell NU substrate are shown in Fig. 4. The spin-coating parameters were set with reference to our previous work (1000 rpm, 1 min). The spectra were recorded using the proposed

reflection mode detection system, using the detectable spectral range from 450 to 1000 nm. As illustrated, after MISG layer coating, both of the spectral peaks λ_2 and λ_3 were blue-shifted (Fig. 4(a)). Before MISG layer coating, the absorbance intensity of the second peak (λ_2) was stronger than the third spectral peak (λ_3), while after MISG layer coating the second spectral peak intensity decreased and that of the third spectral peak increased. Hence, because of the peak position information, it is speculated that the electric field coupling effect strengthened, which is thought to be beneficial for RIS enhancement. As illustrated in Fig. 4(b), an air flow of hex vapor caused both λ_2 and λ_3 to red-shift. The spectral responses of MISG_{hep} and MISG_{oct} to hep and oct vapors were

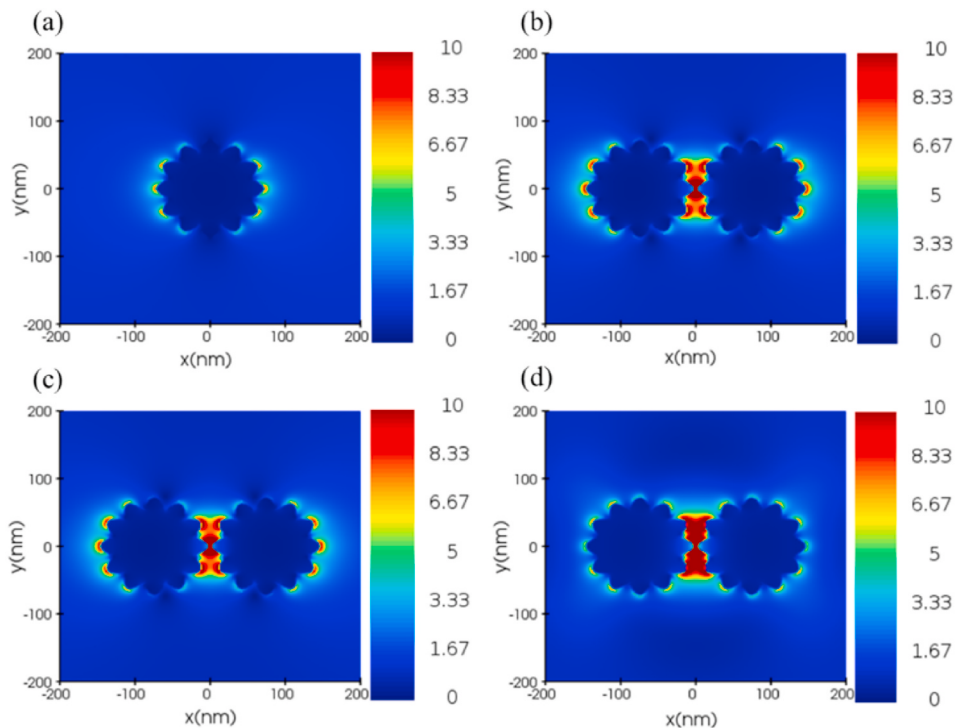


Fig. 3. Electric field distributions of Au@Ag core-shell NU dimer with Ag shell thickness of 2 nm as a (a) monomer and (b–d) dimer (inter-NU distance: 5 nm) (b) on no particular substrate (c) on silica glass and (d) on ITO glass.

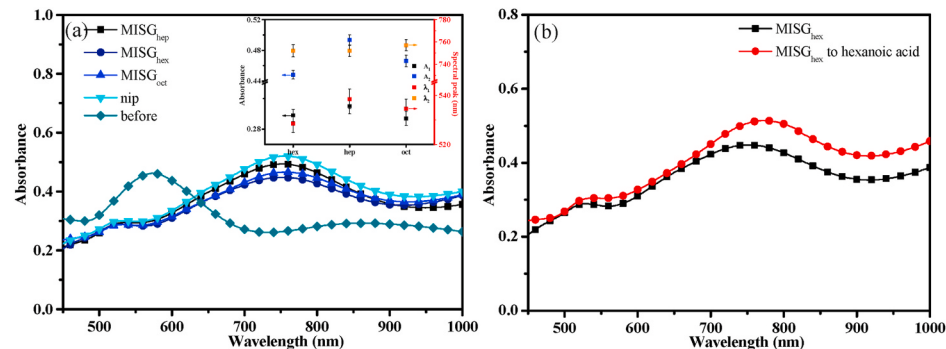


Fig. 4. (a) Absorption spectra of MISG-coated Au@Ag core-shell NUs (spin coating condition: 6 μ L of MISG at 1000 rpm for 1 min) inset: the spectral peaks position and related absorbance after MISG coating (b) Spectral response of MISG_{hex}-coated Au@Ag core-shell NUs to hex vapor.

also tested (Fig. S8), and reflect the same spectral response as shown in Fig. 4(b). Moreover, the spectral response (RIS) of the uncoated Au@Ag core-shell NUs/ITO substrate to the hex vapor with the same concentration was investigated as a reference (Fig. S9). The results show that hex vapor response of MISG-coated Au@Ag core-shell NUs is greater than that of the uncoated substrate, which may be explained by two considerations. The first is that the electric field coupling effect becomes much sounder after MISG coating, and the second is that the MISG layer induces a selective vapor concentration effect. According to the work of Fusco et al. (2018), an optimal aerosol thickness of 1.8 μ m on Au nanodisks leads to a five-fold increase in the shift of the plasmonic resonance, which is explained by the high porosity and surface area of the aerosols. Herein, we posit that the MISG layer provides a unique opportunity for the efficient trapping of gas molecules and the possibility to increase the effective change in RI for LSPR sensing because of the selective absorption of the MISG layer and the cracks on the surface (Fig. S10). To show the response speed and the reusability obviously, absorbance change at the spectral peak (752 nm) was recorded in air and vapor flows versus time (Fig. S11). The response time (time required to

achieve 90% of the maximum response) is about less than 2 s. For hex, hep and oct vapors detection, the sensing range is in tens of ppm level, which is mainly ascribed to the refractive index (RI) sensing volume of Au@Ag core-shell nano-urchins and the effective target vapor molecule binding cavities in MISG matrix.

To evaluate the vapor selectivity of the MISG-LSPR sensors, the spectral response of the sensors was tested in the presence of three primary OA vapors: hex, hep, and oct, as shown in Fig. 5 (a–c), respectively. The largest sensor responses were generated in the corresponding imprinted OA templates. Although the sensor selectivity was verified, interference between sensors still exists. To solve this problem, MISG-LSPR sensors combined with a machine learning method were proposed for further OA vapor identification and classification.

To visualize the clustering trends of different vapors in a low dimension, PCA was performed on the spectral response matrix ($\Delta\lambda_2$ and $\Delta\lambda_3$). The PCA method is an unsupervised method, where the samples were clustered together based only on the similarities and differences in their PC scores (Vera et al., 2011; Zhang et al., 2012). In the PC1-PC2 space (Fig. S12(a)), vapor clusters could be sorted by concentration in

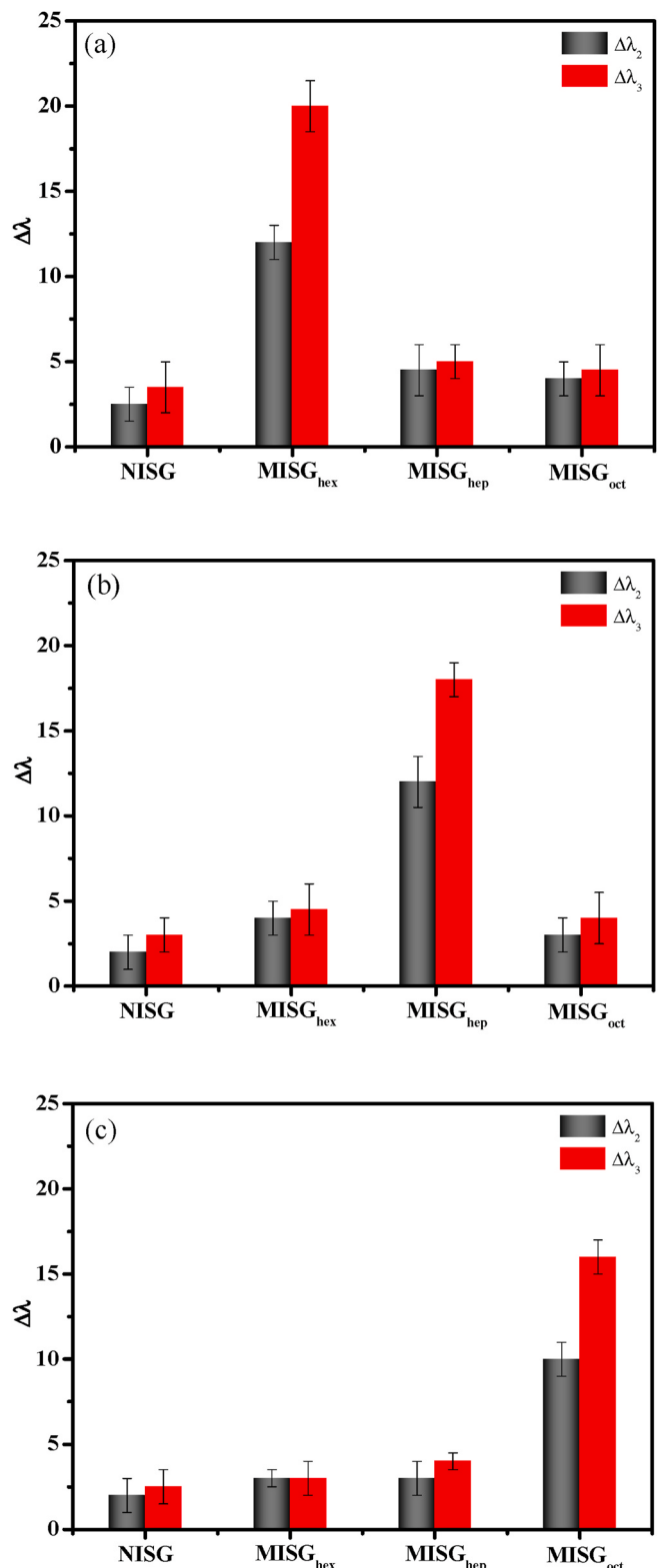


Fig. 5. RIS of NISG, MISG_{hex}, MISG_{hep}, and MISG_{oct} to (a) hex, (b) hep and (c) oct vapors (air flow speed: 0.3 L/min).

descending order. This indicates that the concentration information of vapors and vapor mixtures may be contained in PC1. In addition, we found that the OA mixture samples were clustered in the center region among the single-vapor sources in PC1–PC2 (Fig. S12(a)) and PC2–PC3 (Fig. S12(b)) spaces, though not in the PC1–PC3 space (Fig. S12(c)). This result indicates that balance in the PCA spaces is not totally achieved. In

all PC spaces, the cluster of the single-OA samples and the OA-mixture samples could not be clearly separated. To maximize the variance between groups and minimize the variance within single-OA samples and the OA vapor mixture, the LDA method was applied (Wu et al., 2017; Panigrahi et al., 2006). As shown in Fig. 6, a clear clustering effect of six distinct groups with no overlap was realized, which suggests that the LSPR-MISG sensor combined with the LDA method is applicable to recognize and classify single or mixed vapors. Moreover, to improve the OA vapor classification ability, KNN and NB classification frames were investigated, whose performance evaluation parameters are summarized in Table S1.

The KNN method has been widely applied as a supervised pattern recognition approach because of its robust nature and suitability for limited sample sets (Adeniyi et al., 2016; Acharya et al., 2017). The main assumption of KNN is that increased closeness between samples is directly related to the likelihood they belong in the same category. According to the classification performance and the size of the sample response matrix, the three nearest neighbors ($K = 3$) were chosen in this work. The NB method is a supervised statistical model established by calculating the probability that a given sample belongs to a certain class (Jiang et al., 2018; Saritas and Yasar, 2019). In this study, 54 samples were divided into training and testing sets using the random selection method, where the ratio of samples in the training and testing sets was set to be 3:1. To improve the stability performance of the model, the sample partition process was repeated 100 times. The identification performance of the classification method was evaluated by accuracy, as shown in Table S1.

For each OA, the LDA model showed the highest average accuracy in identifying hex (99.58%) and hep (99.5%) vapors. The NB model demonstrated the highest average accuracy in oct (99.02%), Hex + Hep (99.17%), Hex + Oct (98.28%), and Hep + Oct (98.38%) vapor identification. This result indicates that the NB model is the most suitable for dealing with complicated samples. According to the total average accuracy, NB exhibited the highest accuracy (98.84%), followed by LDA (98.10%) and then KNN (95.75%). In general, it was found that NB was the optimal model to identify OA vapors. In addition, the lowest accuracy achieved by the models was higher than 95%, which reflected that enough molecular information was successfully captured by the MISG-LSPR sensors to realize OA vapor identification. Although these proposed sensors realized OA vapor identification, molecular information captured by the sensors is still insufficient to deal with the complicated OA vapors of real samples. We postulate that the identification of complicated vapor mixtures will be possible by developing more types of

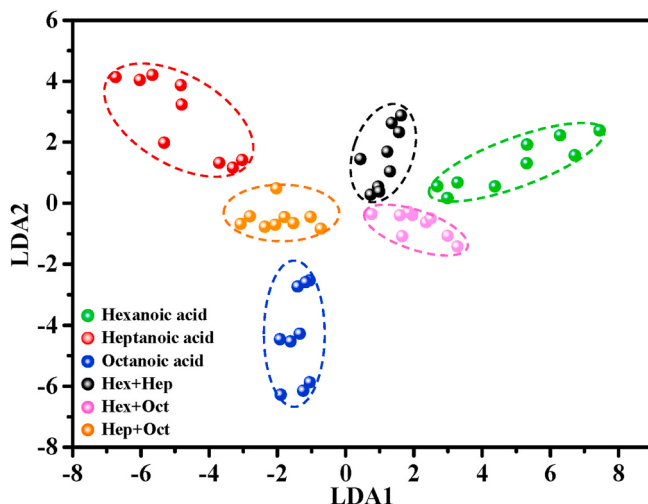


Fig. 6. LDA score plot of the first three discriminant factors achieved from the response matrix of 54 samples from three OAs (hex, hep, oct) and their mixtures (Hex + Hep, Hex + Oct and Hep + Oct).

MISG-LSPR sensors.

4. Conclusions

In summary, an optical fiber-based reflection mode sensing system was proposed based on MISG-LSPR sensors for OA vapor detection. Compared with LSPR sensors in the transmission mode proposed in our previous work, the experimental results in this work demonstrated that the device designed in the reflection mode exhibited comparable sensitivity and selectivity. The Au@Ag core-shell NPs were synthesized and deposited on ITO glass, which demonstrated a significantly enhanced RIS. The MISG and NISG solutions were spin-coated on the optimized films as MISG-LSPR sensors to generate a specific selectivity to the three types of biogenetic OA vapors, including hex, hep, and oct. The normalized vapor responses of the MISG-LSPR sensors to OA vapors exhibited selectivity to the corresponding template molecules. Finally, the PCA, LDA, KNN, and NB methods were used to divide the single- and mixed OA vapors into clusters based on a vapor-sensing matrix. The NB and LDA methods exhibited a satisfactory performance for vapor classification, which verified that it is possible to apply the MISG-LSPR sensors toward practical pattern recognition of single or mixed vapors.

CRediT authorship contribution statement

Bin Chen: Conceptualization, Methodology, Software, Investigation, Writing - original draft. **Hao Guo:** Software, Validation. **Chuanjun Liu:** Writing - review & editing. **Liang Shang:** Investigation. **Xiao Ye:** Investigation. **Lin Chen:** Data curation. **Changhao Feng:** Writing - review & editing. **Kenshi Hayashi:** Supervision.

Declaration of competing interest

The authors declare that they have no known competing financial interests or personal relationships that could have appeared to influence the work reported in this paper.

Acknowledgements

This study was supported by National Nature Science Foundation of China No. 61801400, No. 61703348, JSPS KAKENHI Grant Number JP18F18392, Central Universities under Grant numbers XDKJ2018C021.

Appendix A. Supplementary data

Supplementary data to this article can be found online at <https://doi.org/10.1016/j.bios.2020.112639>.

References

Acharya, U.R., Bhat, S., Koh, J.E.W., Bhandary, S.V., Adeli, H., 2017. Comput. Biol. Med. 88, 72–83.

- Adeniyi, D.A., Wei, Z., Yongquan, Y., 2016. Appl. Comput. Inform. 12, 90–108.
- Chen, B., Liu, C., Ge, L., Hayashi, K., 2016a. Sensor. Actuator. B Chem. 231, 787–792.
- Chen, B., Liu, C., Xie, Y., Jia, P., Hayashi, K., 2016b. IEEE Sensor. J. 16 (10), 3532–3540.
- Chen, L., Huang, Y., Xing, T.T., Ge, L., Yang, T., Chen, B., Huang, C.Z., 2017. J. Mater. Chem. C 5, 7806–7812.
- Chen, B., Liu, C., Shang, L., Guo, H., Qin, J., Ge, L., Jing, C.J., Feng, C., Hayashi, K., 2020. J. Mater. Chem. C 8, 262–269.
- Ciraci, C., Hill, R.T., Mock, J.J., Urzumov, Y., Fernández-Domínguez, A.I., Maier, S.A., Pendry, J.B., Chilkoti, A., Smith, D.R., 2012. Science 337, 1072–1074.
- Fusco, Z., Rahmani, M., Bo, R., Verre, R., Motta, N., Käll, M., Neshev, D., Tricoli, A., 2018. Adv. Mater. 30, 1800931–1800942.
- Halas, N.J., Lal, S., Chang, W.S., Link, S., Nordlander, P., 2011. Chem. Rev. 111, 3913–3961.
- Jiang, W.Q., Shen, Y.F., Ding, Y.F., Ye, C.Y., Zheng, Y., Zhao, P., Liu, L.L., Tong, Z., Zhou, L.F., Sun, S., Zhang, X.C., Teng, L.S., Timko, M.P., Fan, L.J., Fang, W.J., 2018. Int. J. Canc. 142, 357–368.
- Kim, H.M., Jeong, D.H., Lee, H.Y., Park, J.H., Lee, S.K., 2019. Optic Laser. Technol. 114, 171–178.
- Kolk, A.H., van Berkel, J.J., Claassens, M.M., Walters, E., Kuijper, S., Dallinga, J.W., 2012. Int. J. Tubercul. Lung Dis. 16, 777–782.
- Kong, Q., Wang, Y., Zhang, L., Ge, S., Yu, J., 2017. Sensor. Actuator. B Chem. 243, 130–136.
- Lederer, A.K., Pisarski, P., Kousoulas, L., Feigl, S.F., Hess, C., Huber, R., 2017. BMC Surg. 17, 125–135.
- Lee, B., Park, J.H., Byun, J.Y., Kim, J.H., Kim, M.G., 2018. Biosens. Bioelectron. 102, 504–509.
- Liu, C., Shang, L., Yoshioka, H., Chen, B., Hayashi, K., 2018. Anal. Chim. Acta 1010, 1–10.
- Mayer, K.M., Hafner, J.H., 2011. Chem. Rev. 111, 3828–3857.
- Miekisch, W., Schubert, J.K., Noeldge-Schomburg, G.F., 2004. Clin. Chim. Acta 347, 25–39.
- Mock, J.J., Hill, R.T., Tsai, Y.J., Chilkoti, A., Smith, D.R., 2012. Nano Lett. 12, 1757–1764.
- Pai, J.H., Yang, C.T., Hsu, H.Y., Wedding, A.B., Thierry, B., 2017. Anal. Chim. Acta 974, 87–92.
- Panigrahi, S., Balasubramanian, S., Gu, H., Logue, C.M., Marchello, M., 2006. Sensor. Actuator. B Chem. 119, 2–14.
- Saritas, M.M., Yasar, A., 2019. Int. J. Intell. Syst. 7 (2), 88–91.
- Shang, L., Liu, C., Chen, B., Hayashi, K., 2018a. Sensor. Actuator. B Chem. 260, 167–626.
- Shang, L., Liu, C., Chen, B., Hayashi, K., 2018b. ACS Sens. 3, 1531–1538.
- Shen, Y., Zhou, J., Liu, T., Tao, Y., Jiang, R., Liu, M., Xiao, G., Zhu, J., Zhou, Z.K., Wang, X., Jin, C., Wang, J., 2013. Nat. Commun. 4, 1–9.
- Tiwari, M.P., Prasad, A., 2015. Anal. Chim. Acta 853, 1–18.
- Tsoukalas, D., Alegakis, A., Fragkiadaki, P., Papakonstantinou, E., Nikitovic, D., Karataraki, A., Nosyreva, A.E., Papadakis, E.G., Spandidos, D.A., Drakoulis, N., Tsatsakis, A.M., 2017. Int. J. Mol. Med. 40, 112–120.
- Usami, M., Miyoshi, M., Kanbara, Y., Aoyama, M., Sakaki, H., Shuno, K., Hirata, K., Takahashi, M., Ueno, K., Tabata, S., Asahara, T., Nomoto, K., 2011. JPEN - J. Parenter. Enter. Nutr. 35 (3), 317–328.
- Uzun, L., Turner, A.P.F., 2016. Biosens. Bioelectron. 76, 131–144.
- Vera, L., Acena, L., Guasch, J., Boque, R., Mestres, M., Bustos, O., 2011. Anal. Bioanal. Chem. 399, 2073–2081.
- Wackerlig, J., Schirhagl, R., 2016. Anal. Chem. 88, 250–261.
- Willets, K.A., Duyne, R.P.V., 2007. Annu. Rev. Phys. Chem. 58, 267–297.
- Wu, L., Shen, C., Hengel, A.V.D., 2017. Pattern Recogn. 65, 238–250.
- Wustholz, K.L., Henry, A.I., McMahon, J.M., Freeman, R.G., Valley, N., Piotti, M.E., Natan, M.J., Schatz, G.C., Duyne, R.P.V., 2010. J. Am. Chem. Soc. 132, 10903–10910.
- Yan, X., Li, H., Su, X., 2018. Trends Anal. Chem. 103, 1–20.
- Yokoyama, Y., Mizuno, T., Sugawara, G., Asahara, T., Nomoto, K., Igami, T., Ebata, T., Nagino, M., 2017. Surgery 162 (4), 928–936.
- Zhang, X.J., You, L., Anslyn, E.V., Qian, X.H., 2012. Chem. Eur. J. 18, 1102–1110.
- Zhang, J., Wang, C., Niu, Y., Li, S., Luo, R., 2017. Sensor. Actuator. B Chem. 249, 747–755.